The Astrophysical Journal, 631:733–740, 2005 October 1

A *CHANDRA* HETGS SPECTRAL STUDY OF THE IRON K BANDPASS IN MCG −6-30-15: A NARROW VIEW OF THE BROAD IRON LINE

A. J. Young,[1] J. C. Lee,[2,3] A. C. Fabian,[4] C. S. Reynolds,[5] R. R. Gibson,[1] and C. R. Canizares[1]

Received 2005 February 7; accepted 2005 May 30

ABSTRACT

We present a high-resolution X-ray spectrum of the iron K bandpass in MCG −6-30-15 based on a 522 ks observation with *Chandra*'s High Energy Transmission Grating Spectrometer (HETGS). The *Chandra* spectrum is consistent with the presence of a relativistically broadened, highly redshifted iron Kα emission line with a profile similar to previous observations. A number of narrow features are detected above 2 keV, including a narrow Fe Kα emission line and narrow absorption lines from H- and He-like Fe, H-like S, and H-like Si. This absorption is well described by a photoionized plasma with a column density $\log N_{\rm H} = 23.2$ and an ionization parameter $\log \xi = 3.6$, assuming the iron abundance has the solar value and a velocity dispersion parameter $b = 100$ km s^{-1}. Applying this absorption model to a high-fidelity *XMM-Newton* EPIC pn spectrum, we find that a broad iron line is still required with emission extending to within $1.9r_g$ of the black hole. If the iron line comes from an accretion disk truncated at the innermost stable circular orbit, this indicates that the black hole must be spinning rapidly with $a > 0.95$. Ionized absorption models attempting to explain the 3–6 keV spectral curvature without strong gravity predict absorption lines in the 6.4–6.6 keV range that are inconsistent with the *Chandra* spectrum. The H- and He-like iron absorption lines in the *Chandra* spectrum are blueshifted by $2.0^{+0.7}_{-0.9} \times 10^3$ km s^{-1} compared to the source frame and may originate in a high-velocity, high-ionization component of the warm absorber outflow. This high-ionization component may dominate the energy budget of the outflow and account for a significant fraction of the outflowing mass. Detailed modeling of the warm absorber below 2 keV will be addressed in a later paper, but our results are robust to the broader details of the warm absorber behavior. The difference spectrum between the high- and low-flux states is well described by a power law, in agreement with previous studies.

Subject headings: accretion, accretion disks — black hole physics — galaxies: active — galaxies: individual (MCG −6-30-15) — galaxies: Seyfert — X-rays: galaxies

Online material: color figures

1. INTRODUCTION

Efficiently accreting black holes are prodigious sources of X-rays. The illumination of a dense thin accretion disk with X-rays inevitably leads to the production of a strong iron fluorescence line (Fabian et al. 1989; Nandra et al. 1989). If the accretion disk lies deep in the potential well of the black hole, the fluorescent iron line profile will be broadened and skewed in a characteristic manner by the Doppler and transverse Doppler shifts of the high-velocity orbiting gas and the gravitational redshift and light focusing of the black hole (see, e.g., the review articles by Fabian et al. 2000; Reynolds & Nowak 2003). As such, the broad iron line is potentially a powerful probe of the astrophysics and spacetime in the immediate vicinity of a black hole. A major *Advanced Satellite for Cosmology and Astrophysics* (*ASCA*) discovery was just such a line at 6.4 keV from Fe Kα in the Seyfert 1 galaxy MCG −6-30-15 (Tanaka et al. 1995), which showed broadening as large as $\sim$100,000 km s^{-1}. Subsequent studies of other active galactic nuclei (AGNs) have reinforced the existence of broad lines (Mushotzky et al. 1995; Nandra et al. 1997).

The broad iron line in MCG −6-30-15 has been extensively studied with *ASCA* (Iwasawa et al. 1996, 1999; Shih et al. 2002), *BeppoSAX* (Guainazzi et al. 1999), the *Rossi X-Ray Timing Explorer* (*RXTE*; Lee et al. 1999, 2000; Vaughan & Edelson 2001), the *Chandra X-Ray Observatory* (Lee et al. 2002b) and the *X-Ray Multi-Mirror* mission (*XMM-Newton*: Wilms et al. 2001; Fabian et al. 2002; Vaughan & Fabian 2004; Reynolds et al. 2004). All observations are consistent with a broad, highly redshifted disk line feature. Most alternative mechanisms for broadening the iron emission line (i.e., those that do not require strong gravity) are unlikely to work (e.g., Fabian et al. 1995; Reynolds & Wilms 2000; Ruszkowski et al. 2000). We present a deep *Chandra* High Energy Transmission Grating Spectrometer (HETGS) observation of MCG −6-30-15 and, concentrating on the iron K bandpass, describe the narrow emission and absorption features in the spectrum above 2 keV, constrain the column densities and ionization parameters of highly ionized absorbing gas, and discuss the implications. We investigate whether the broad iron line is not an emission feature but the result of a curved continuum spectrum caused by ionized absorption (e.g., Kinkhabwala 2003). Detailed modeling of the warm absorber below 2 keV will be addressed in a later paper, and our results are robust to the broader details of the warm absorber behavior.

2. OBSERVATIONS

MCG −6-30-15 ($z = 0.007749$) was observed by the *Chandra* HETGS between 2004 May 19 and 27 (obs/4759, obs/4760, obs/4761, and obs/4762), resulting in a good exposure time of

[1] Massachusetts Institute of Technology Center for Space Research, 77 Massachusetts Avenue, Cambridge, MA 02139.
[2] Harvard-Smithsonian Center for Astrophysics, 60 Garden Street, MS-4, Cambridge, MA 02138.
[3] *Chandra* Fellow.
[4] Institute of Astronomy, University of Cambridge, Madingley Road, Cambridge CB3 0HA, UK.
[5] Department of Astronomy, University of Maryland, College Park, MD 20742.

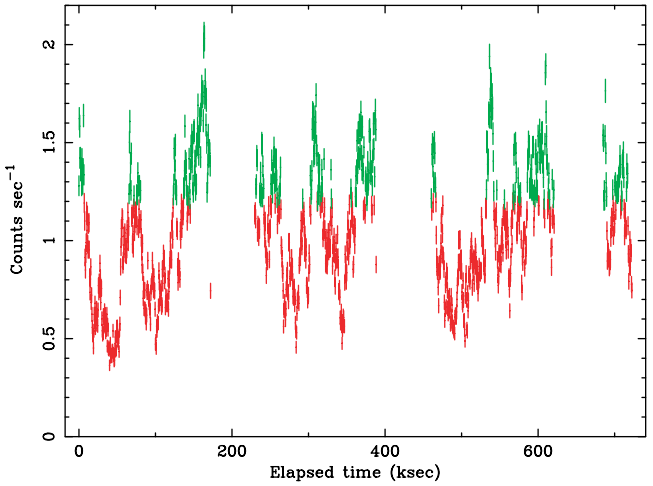

FIG. 1.—Combined HEG plus MEG 0.45–10 keV first-order light curve of MCG −6-30-15. The high- (*green*) and low- (*red*) flux states are separated by 1.2 counts s^{-1}.

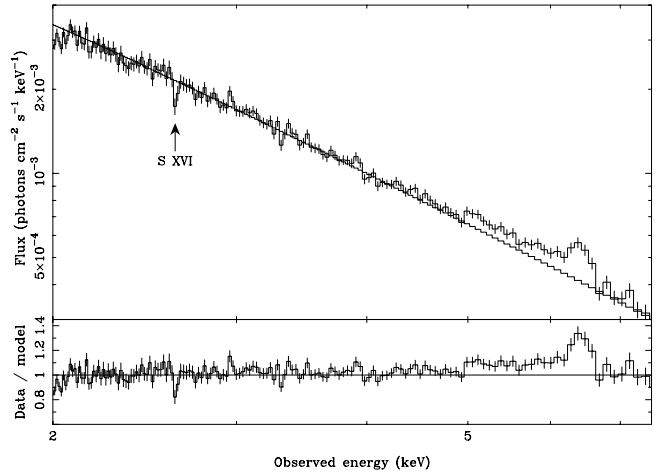

FIG. 2.—Heavily binned HEG spectrum of MCG −6-30-15 (*top*) with a power law joining the 2.5–3 and 8–9 keV bands overlaid (*solid line*) and the ratio of the data to power-law model (*bottom*). The heavy binning reveals the broad iron Kα line that peaks around 6.4 keV and is extremely redshifted down to $\lesssim$5 keV. The arrow indicates S XVI Lyα absorption at 2.62 keV. [*See the electronic edition of the Journal for a color version of this figure.*]

522 ks. Spectra and instrument responses were generated using the standard CIAO tools and analyzed using the ISIS spectral fitting software (Houck 2002). For improved accuracy, we correct the individual S0–S5 chip effective areas (ancillary response functions [ARFs]) before combining them to generate the medium-energy gratings (MEG) and high-energy gratings (HEG) +1 and −1 effective areas used for data analysis. To do so, we correct the quantum efficiencies (QEs) of the S0, S2, S4, and S5 front-illuminated (FI) chips to better agree with the QEs of the back-illuminated (BI) S1 and S3 chips using a publicly available correction factor (Marshall et al. 2004).[6] The correction is <10% above 900 eV and <19% below. Once corrected, the CIAO tool `dmarfadd` was used to combine the S0–S5 effective areas to create the −1 and +1 ARFs. The +1 and −1 orders of the HEG were combined, as were the +1 and −1 orders of the MEG. The HEG and MEG spectra were modeled separately. The zeroth-order spectrum is heavily piled up ($\gtrsim$90% given an observed zeroth-order rate of $\simeq$0.7 counts per frame) and is not used. The combined HEG plus MEG first-order 0.45–10 keV count rate varies between $\simeq$0.4 and 2 counts s^{-1}, and the light curve is shown in Figure 1. The error bars quoted throughout the paper are the 90% confidence interval ($\Delta\chi^2 = 2.706$ for one interesting parameter), unless explicitly stated otherwise.

2.1. *Broad Iron Line*

To show the broad iron line, the high-resolution HEG spectrum was heavily binned to 0.067 Å bin^{-1}, and an absorbed power-law model was used to join the 2.25–2.5 and 7–7.5 keV bands (see Fig. 2). The best-fit photon index is $\Gamma = 1.82^{+0.05}_{-0.04}$, with the neutral absorbing column density fixed at $N_{\rm H} = 2.1 \times 10^{21}$ cm^{-2} to approximate the effects of the warm absorber (a few percent above $\simeq$3 keV; Lee et al. 2001).

The broad iron line profile is very similar to that seen in previous observations, and a comparison between the *Chandra* and *XMM-Newton* (Vaughan & Fabian 2004) line profile is shown in Figure 3. The "red wing" of the iron K line extends from $\simeq$6 keV down to $\lesssim$3–5 keV, and the "narrow core" peaks around 6.4 keV. The *XMM-Newton* spectrum has a slightly different continuum model, namely, an absorbed power law joining the 2–3 and 8.5–10 keV bands with neutral $N_{\rm H} = 3.6 \times 10^{21}$ cm^{-2} and $\Gamma = 1.98$. There is remarkable agreement between the *Chandra* and *XMM-Newton* spectra even though they were not contemporaneous.

The continuum and broad iron line in the *Chandra* HEG spectrum are well described (χ^2/dof = 144/123) by a relativistic disk line plus reflection model. The reflection spectrum is modeled by PEXRAV (Magdziarz & Zdziarski 1995) plus a narrow Gaussian fixed at 6.4 keV in the source frame. The PEXRAV model spectrum consists of two components, a power law plus a "reflected" or backscattered continuum that is produced by a power-law spectrum illuminating a slab of neutral gas. The PEXRAV model does not include the iron fluorescence line, and hence that is added as a narrow Gaussian at 6.4 keV. The reflection fraction (the ratio of

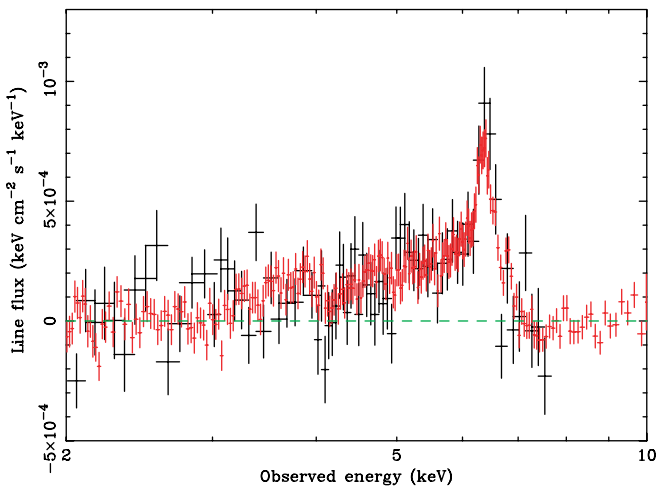

FIG. 3.—MCG −6-30-15 broad iron line from *Chandra* HEG (*black points*) and *XMM-Newton* EPIC pn (Vaughan & Fabian 2004; *red points*) shown in flux units. The *Chandra* data have been heavily binned (0.03 Å bin^{-1} above 4 keV and more heavily below 4 keV). This plot was created by taking the ratio of each data set to the appropriate underlying power-law continuum model (see § 2.1) and multiplying by the power-law model normalization. There is excellent agreement between the broad iron line profiles even though the *Chandra* and *XMM-Newton* observations were not contemporaneous. The red wing of the iron K line extends from $\simeq$6 keV down to $\lesssim$3–5 keV, and the narrow core peaks around 6.4 keV.

[6] A BI:FI correction file is available at http://space.mit.edu/ASC/calib/ficorr.txt.

TABLE 1
CONTINUUM AND IRON LINE PARAMETERS

N_H[a] (cm^{-2})	Γ	K[b]	r_{in} (r_g)	r_{out}[a] (r_g)	q[c]	i (deg)	EW (Broad) (eV)	EW (Narrow) (eV)	χ^2/dof
2.1×10^{21}.....	1.94 ± 0.01	1.6×10^{-2}	$1.3^{+12.5}_{-0.1}$	200	$2.3^{+2.5}_{-0.1}$	26^{+3}_{-4}	134^{+64}_{-11}	15^{+10}_{-9}	144/123

NOTES.—The reflection fraction R is fixed at 2.2, and the iron abundance A_{Fe} is fixed at 3 times the solar value based on previous *XMM-Newton* observations (Fabian et al. 2002). The broad Fe Kα line energy is fixed at a source frame energy of 6.40 keV.
[a] Parameter fixed.
[b] The normalization of the PEXRAV model, K = photons cm^{-2} s^{-1} keV^{-1}, of the power-law component at 1 keV in the observed frame.
[c] The radial emissivity profile of the disk line is $\propto r^{-q}$.

the normalization of the reflected spectrum to the normalization of the power law, with a value of 1 for an isotropic source above the disk) is fixed at 2.2, and the iron abundance is fixed at 3 times the solar value based on previous *XMM-Newton* models (Fabian et al. 2002). Both the reflection and iron line component are blurred by a disk line kernel for emission around a spinning Kerr black hole (Laor 1991), and everything is absorbed by a fixed neutral column density. In addition, a narrow, neutral Fe Kα line is added at 6.4 keV in the source frame to represent reflection off distant material, e.g., the narrow-line region or torus. The model parameters are given in Table 1.

The HETGS spectrum is best suited to studying narrow spectral features and does not strongly constrain the broad-line properties. A model in which the reflection fraction is fixed at $R = 1$ and the iron abundance fixed at the solar value also provides a good description of the spectrum with similar broad iron line parameters and an almost identical χ^2/dof of 143/123. Since we cannot easily distinguish between such broadband models, we have adopted the values used by Fabian et al. (2002; i.e., $R = 2.2$ and an iron abundance of 3 times the solar value), and the line energies and equivalent widths (EWs) we measure are insensitive to this choice. We can, however, show that the HEG spectrum is better described by a neutral broad iron line than an ionized broad iron line. If the iron line added to the reflection spectrum is at 6.7 keV instead of 6.4 keV, the best-fit model has a worse χ^2/dof = 152/123. We do not include the weak reflection continuum associated with the narrow 6.4 keV line, and this does not affect our results.

2.2. *Narrow Iron Line Components*

The unbinned HEG spectrum (0.0056 Å bin^{-1}; the FWHM of the HEG is 0.012 Å) shows a number of narrow emission and absorption features in the iron K bandpass (Fig. 4). The 5.5–7.5 keV continuum and broad iron line were modeled as described in § 2.1 and Table 1, with most of the parameters fixed except the normalizations of the continuum and broad line and the parameters of the Gaussian representing the neutral Fe Kα line. Individual absorption lines were added as Gaussians with their centroids, strengths, and widths being free parameters. The best-fit line parameters are given in Table 2.

There is a narrow emission line at 6.39 keV (source frame), consistent with neutral iron Kα fluorescence, that has an EW of 18 eV (in good agreement with Lee et al. 2002b) and a FWHM of <4700 km s^{-1}. We also detect two unresolved absorption features, one at 6.69 keV (observed) consistent with the $1s$–$2p$ resonance line of He-like iron (6.70 keV; Verner et al. 1996) and the second at 6.96 keV (observed) consistent with the two $1s$–$2p$ resonance lines of H-like iron (6.95 and 6.97 keV; Verner et al. 1996). Both of these absorption features are consistent with zero redshift or, if associated with MCG −6-30-15, an outflow velocity of $2.0^{+0.7}_{-0.9} \times 10^3$ km s^{-1} for Fe XXV and $1.9^{+0.7}_{-0.8} \times 10^3$ km s^{-1} for Fe XXVI.

2.3. *Variability*

We now compare the spectrum of MCG −6-30-15 in a high- and low-flux state, since this can help determine whether certain spectral features are caused by absorption or emission. Using the combined first-order HEG plus MEG light curve of MCG −6-30-15 with 500 s bins (Fig. 1), we extracted high- and low-flux state spectra from those bins with count rates greater than or less than 1.2 counts s^{-1}, respectively. The effective exposure times are 172 ks for the high-flux state and 350 ks for the low-flux state, chosen so that the signal-to-noise ratio of each spectrum is comparable. The high- and low-flux state HEG spectra are shown in Figure 5, and the parameters of the narrow iron emission and absorption lines are given in Table 2. The line centroid energies are consistent between the high- and low-flux states. The difference in the continuum spectrum between the high- and low-flux states in the 2.25–7 keV band is well described ($\chi^2_\nu = 0.9$) by a power law of photon index $\Gamma = 2.0^{+0.2}_{-0.1}$ (see Fig. 6), in agreement with previous findings that the variability is dominated by a power-law component (e.g., Fabian et al. 2002; Turner et al. 2003; Fabian & Vaughan 2003; Vaughan & Fabian 2004). Furthermore, there is no evidence of continuum curvature or systematic deviation

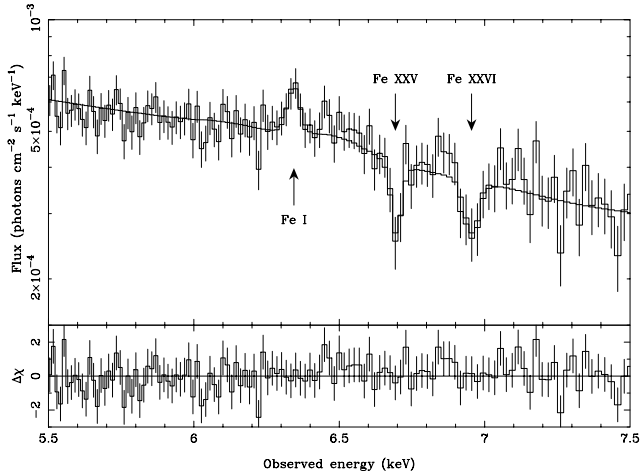

FIG. 4.—MCG −6-30-15 *Chandra* HEG spectrum of the iron K bandpass for the entire observation. The HEG ±1 orders have been combined, and there are 0.0056 Å bin^{-1}. The top panel shows the data (*histogram*) and best-fitting model folded through the instrument response (*solid line*), and the bottom panel shows the χ residuals to the fit. Note the narrow Fe Kα emission at 6.34 keV and the narrow absorption features at 6.69 and 6.96 keV. The underlying continuum model consists of a reflection component plus a neutral Fe Kα line, and both components have been blurred using a relativistic disk line kernel. [*See the electronic edition of the Journal for a color version of this figure.*]

TABLE 2
NARROW EMISSION AND ABSORPTION FEATURES

Flux State	Identification	Laboratory Energy[a] (keV)	Line Energy (keV) Source Frame (Observed)[b]	FWHM (1000 km s^{-1})	EW (eV)
Average	Si XIV	2.01	$2.005(1.990)^{+0.001}_{-0.005}$	<0.7	-2^{+0}_{-1}
	S XVI	2.62	$2.640(2.620)^{+0.006}_{-0.004}$	<3.7	-5^{+2}_{-2}
	Fe I–Fe XIX	6.40–6.47	$6.393(6.344)^{+0.106}_{-0.014}$	<4.7[c]	18^{+11}_{-8}
	Fe XXV	6.70	$6.745(6.693)^{+0.018}_{-0.006}$	<2.0	-18^{+7}_{-5}
	Fe XXVI	6.95, 6.97	$7.009(6.955)^{+0.018}_{-0.017}$	<3.8	-21^{+10}_{-11}
Low	Fe I–Fe XIV	6.40–6.41	$6.407(6.367)^{+0.008}_{-0.016}$	<2.7	25^{+10}_{-9}
	Fe XXV	6.70	$6.745(6.693)^{+0.017}_{-0.021}$	<3.2	-13 ± 9
	Fe XXVI	6.95, 6.97	$7.028(6.974)^{+0.049}_{-0.042}$	<9.0	-23^{+15}_{-20}
High	Fe I	6.40	$6.372(6.323) \pm 0.017$	<2.6	19 ± 11
	Fe XXV	6.70	$6.762(6.710)^{+0.001}_{-0.019}$	<2.3	-25 ± 9
	Fe XXVI	6.95, 6.97	$7.003(6.949)^{+0.018}_{-0.017}$	$2.0^{+1.8}_{-1.7}$	-32^{+14}_{-16}

[a] Values for He- and H-like ions from Verner et al. (1996), and values for Fe I–Fe XIX from House (1969).
[b] The first figure gives the line energy in the source frame, and the second figure (in parentheses) gives the observed line energy.
[c] In this case the line energy was fixed at the best-fit value. If the line energy is a free parameter, there is an ambiguity distinguishing between the broad- and narrow-line components, and the FWHM is only weakly constrained to be $<21.8 \times 10^3$ km s^{-1}.

from a power-law model in the 2.25–7 keV band. A narrow He-like iron absorption feature is weakly detected at approximately 6.7 keV in the difference spectrum.

3. DISCUSSION

3.1. *Column Densities*

We can estimate the column densities of Fe XXV and Fe XXVI ions from the EWs of their absorption lines (see, e.g., Spitzer 1978; Kotani et al. 2000). The inferred column density depends on the absorption line profile, and we assume the absorber has a Maxwellian velocity dispersion with a velocity spread parameter $b = \sqrt{2}\sigma$, where σ is the radial velocity dispersion. The thermal broadening is roughly $b \simeq 20$ km s^{-1} for reasonable temperatures, so larger values of b will imply some bulk motion or turbulence in the absorber(s). The column of Fe XXV required to produce an 18 eV EW absorption line is $N_{\rm Fe\ XXV} \simeq (3 \times 10^{17})$–$(3 \times 10^{18})$ cm^{-2} for $b = 500$–100 km s^{-1}, respectively. Similarly, the column density of Fe XXVI required to produce a 21 eV EW absorption line is $N_{\rm Fe\ XXVI} \simeq (6 \times 10^{17})$–$(4 \times 10^{19})$ cm^{-2} for $b = 500$–100 km s^{-1}, respectively. The corresponding hydrogen column density depends on the iron abundance and fraction of iron in each ionization state. For Fe XXV we estimate $N_{\rm H} \simeq (0.5/X_{25})[(n_{\rm H/Fe})/3 \times 10^4](2 \times 10^{22})$–$(2 \times 10^{23})$ cm^{-2} for $b = 500$–100 km s^{-1}, respectively, where $n_{\rm H/Fe}$ is the ratio of hydrogen ions to all iron ions (3×10^4 for solar abundance) and X_{25} is the fraction of iron ions found in Fe XXV (which peaks around 0.5). Similarly, for Fe XXVI we infer $N_{\rm H} \simeq (0.5/X_{26})[(n_{\rm H/Fe})/3 \times 10^4](4 \times 10^{22})$–$(3 \times 10^{24})$ cm^{-2} for $b = 500$–100 km s^{-1}, respectively. If the H- and He-like Fe absorption lines are produced in a single absorber with $\log \xi \simeq 3.5$–4, then $X_{25} \simeq X_{26} \simeq 0.4$–0.5 (see Fig. 8 of Kallman & Bautista 2001).

If we model the absorbing gas as a photoionized plasma illuminated by a power law using the XSTAR code (Kallman & Bautista 2001), with solar iron abundance and $b = 100$ km s^{-1}, a good fit ($\chi^2_\nu = 1.1$) to the 5.5–7.5 keV spectrum is given by a power law plus disk line plus narrow iron Kα emission line absorbed by a column density $\log N_{\rm H} = 23.2^{+0.3}_{-0.6}$ with an ionization parameter $\log \xi = 3.6^{+0.1}_{-0.2}$, where $\xi = L_{\rm ion}/(n_e R^2)$, $L_{\rm ion}$ is

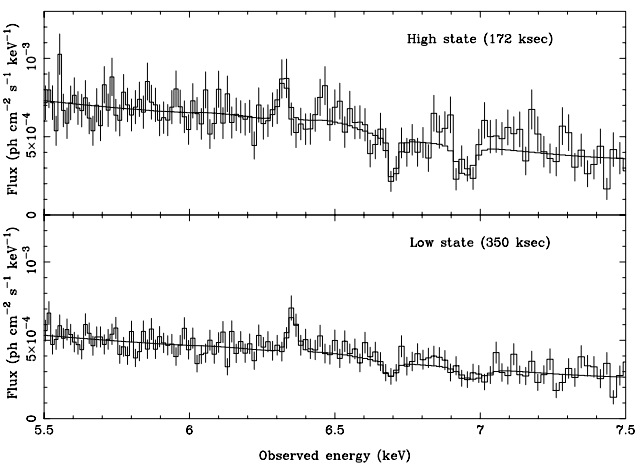

FIG. 5.—MCG −6-30-15 HEG spectra of the iron K bandpass for the high- (*top*) and low-flux states (*bottom*). [*See the electronic edition of the Journal for a color version of this figure.*]

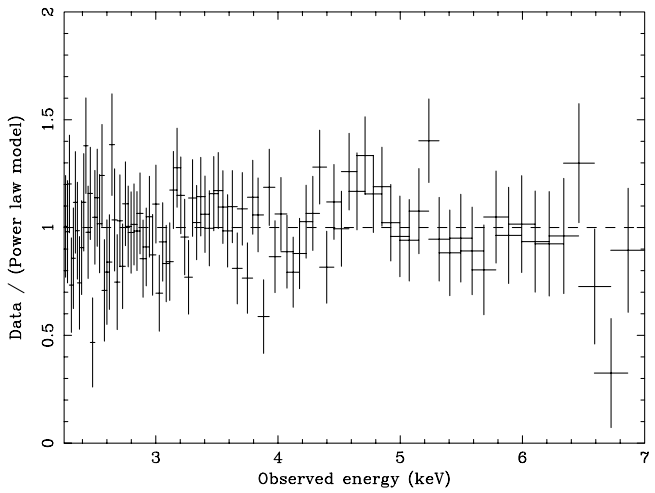

FIG. 6.—Ratio of the difference between the high- and low-flux state spectra to a power-law model with photon index $\Gamma = 2$. Note the suggestion of an absorption line at 6.7 keV. [*See the electronic edition of the Journal for a color version of this figure.*]

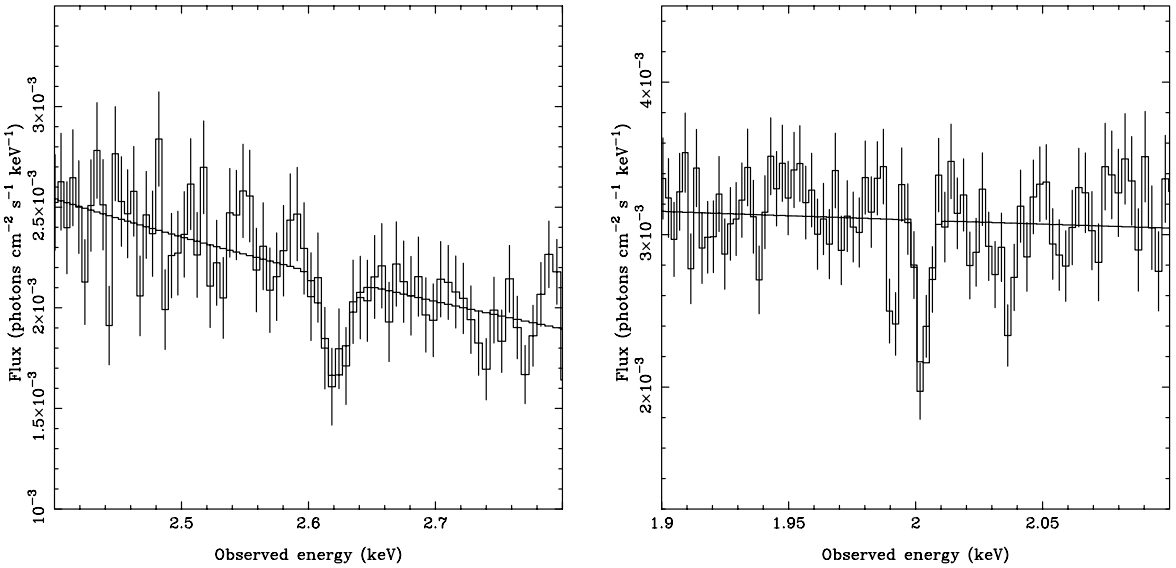

FIG. 7.— *Chandra* HEG spectra showing absorption lines. *Left:* S XVI Lyα absorption (2.62 keV in laboratory frame) outflowing from MCG −6-30-15 at $\simeq$2200 km s^{-1} (*solid line*). *Right:* Si XIV Lyα absorption (2.01 keV in laboratory frame) outflowing from MCG −6-30-15 at $\simeq$2300 km s^{-1} (*solid line*). The absorption feature observed at 1.99 keV is from Si XIV Lyα at rest in the source frame, with an EW of 1 eV. [*See the electronic edition of the Journal for a color version of this figure.*]

the 1–1000 Ryd luminosity, and R is the distance between the continuum source and cloud. For 3 times solar abundance the column density drops to $\log N_{\rm H} = 22.9^{+0.1}_{-1.0}$. The redshift of the absorbing gas is $z = 1.3^{+1.3}_{-1.1} \times 10^{-3}$. Note also that there is some degeneracy between the ionization parameter and b, since both can affect the ratio of Fe XXV EW to Fe XXVI EW. The best-fitting XSTAR model predicts other absorption features that are consistent with the *Chandra* HEG spectrum. The strongest lines predicted by the model in the energy range 2 keV $\lesssim E \lesssim$ 6 keV are S XVI Lyα at 2.62 keV and Si XIV Lyα at 2.01 keV. Both of these absorption lines are detected in the HEG spectrum (Fig. 7; Table 2), with outflow velocities of 2288^{+687}_{-457} km s^{-1} for S XVI and 2247^{+80}_{-726} km s^{-1} for Si XIV. We have not considered in our fit the spectrum below 2 keV or the warm absorber, which will be the subject of a future study. The column densities in the high- and low-flux states are statistically consistent with a single value equal to that of the time-averaged spectrum.

3.2. *Robustness of the Broad Iron Line*

It has been proposed that the extremely redshifted red wing of the iron K line might actually be caused by absorption (e.g., Kinkhabwala 2003). In this model the continuum passes through a large column density of moderately ionized gas, which causes significant curvature of the transmitted continuum above the iron L edge at $\sim$0.7 keV that extends up to the iron K bandpass ($\gtrsim$5 keV), and this curvature can mimic the red wing of the putative broad iron Kα emission line. For iron to have L-shell electrons the absorbing gas cannot be as highly ionized as the gas giving rise to the H- and He-like iron absorption lines. On the other hand, the gas must be sufficiently highly ionized to avoid excessive opacity of soft X-rays; therefore, $\xi \gtrsim 10$–100 (Krolik & Kallman 1984). The fact that the difference spectrum between the high- and low-flux states above 2.25 keV (where the effect of the warm absorber is small) is well described by an unabsorbed power law (§ 2.3) strongly suggests that the curvature is not an absorption artifact. If the curvature in the time-averaged hard X-ray spectrum is caused by an intervening absorber with constant optical depth, $\tau = N\sigma(E)$, then the absorption should affect the intrinsic high state, F_h, and intrinsic low state, F_l, similarly (i.e., as $e^{-\tau}F_h$ and $e^{-\tau}F_l$, respectively), and hence the difference spectrum should also show the same absorption [i.e., $e^{-\tau}(F_h - F_l)$]. We do not expect τ to vary between the high- and low-flux states, since the continuum variability timescale is so short (typically hundreds of seconds). Even though the difference spectrum does not show such an absorption signature above 2.25 keV, in this section we present a comparison between an absorption model and the *Chandra* HEG spectrum.

To test the ionized absorption hypothesis, we modeled the 3–10 keV *XMM-Newton* European Photon Imaging Camera (EPIC) pn spectrum (Vaughan & Fabian 2004) with an XSTAR model absorbing a power-law spectrum, excluding the 6–8 keV range in which the line has a more complicated profile and narrow core (see Fig. 3). The curvature of the broad red wing is approximately described by a model with solar iron abundance, $b = 100$ km s^{-1}, $\log N_{\rm H} = 22.6^{+0.1}_{-0.0}$, $\log \xi = 2.2^{+0.1}_{-0.1}$, and $\Gamma = 2.12^{+0.03}_{-0.02}$. The *XMM-Newton* spectrum was used to construct this model, since it provides better statistical constraints on very broad spectral features than the *Chandra* HEG spectrum. The ionized absorption model predicts a complex of narrow absorption lines between approximately 6.4 and 6.6 keV in the source frame that are inconsistent with the *Chandra* HEG spectrum, as shown in Figure 8. Narrow $1s$–$2p$ iron absorption lines (from Fe XVIII at 6.4 keV up to Fe XXIII at 6.6 keV; Behar & Netzer 2002) are a generic feature of ionized absorption models in which there is significant iron L-shell absorption. We have confirmed that for $b = 0$ km s^{-1} a similarly strong absorption line complex is produced that would be readily visible in the HEG spectrum, and the strength of the absorption lines will increase with increasing b. We conclude that a simple absorption model cannot account for the broad red wing of the iron line.

More complex absorption models are harder to constrain. It is possible that emission lines fill in the absorption lines, although this requires fine-tuning the ionization state and strength of emission so that no significant emission or absorption residuals are seen between $\sim$6.4 and 6.5 keV, and we consider this scenario unlikely. A neutral partial covering model can be ruled out, because it is inconsistent with the *RXTE* spectrum above 10 keV (Reynolds et al. 2004). An ionized partial covering model (e.g., see Turner et al. 2005) cannot simply be ruled out, but if the partial covering component produces a strong absorption line

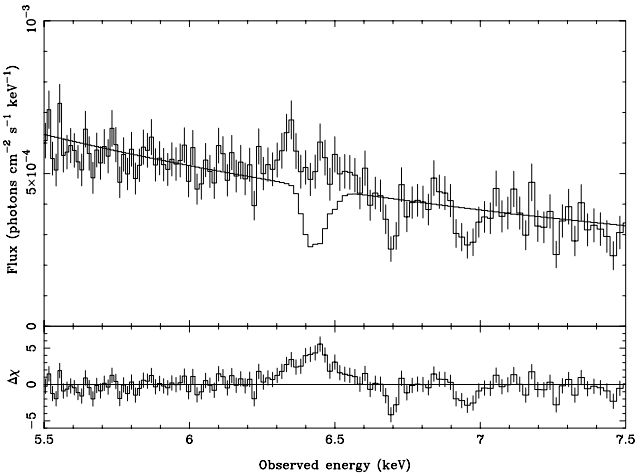

FIG. 8.—*Chandra* HEG spectrum (*histogram with error bars*) with an ionized absorption model (folded through the instrument response) of the broad red wing of the iron line overlaid (*solid line*). The ionized absorber model was fitted to the 3–10 keV *XMM-Newton* spectrum excluding the 6–8 keV range in which the line has a concave profile and narrow core. The ionized absorber produces a curved continuum spectrum but also predicts iron absorption lines in the 6.4–6.6 keV range in the source frame that are inconsistent with the *Chandra* HEG spectrum. We conclude that a simple absorption model cannot account for the broad red wing of the iron line. [*See the electronic edition of the Journal for a color version of this figure.*]

similar to the simple absorption model discussed above, we can constrain the covering fraction to be $f \lesssim 5\%$. For a larger covering fraction the absorption features should be visible in the HEG spectrum. It is difficult to introduce sufficient continuum curvature to account for the red wing of the broad iron line with such a small covering fraction. It is also important to reiterate that the spectral variability of MCG −6-30-15 is inconsistent with an absorption model (§§ 2.3 and 3.2; Fabian et al. 2002).

The presence of the highly ionized absorber giving rise to the H- and He-like iron absorption lines seen in the *Chandra* HEG spectrum at 7.0 and 6.7 keV, respectively, does not significantly affect the modeling of the red wing of the iron K line $\lesssim$6 keV, and hence the conclusion that the black hole must be spinning rapidly is robust. An excellent fit ($\chi^2_\nu = 0.9$) to the 3–10 keV *XMM-Newton* EPIC pn spectrum is given by a power law absorbed by the highly ionized XSTAR model used to describe the *Chandra* HEG spectrum (i.e., solar abundance, $b = 100$ km s^{-1}, $\log N_{\rm H} = 23.2$, $\log \xi = 3.6$) plus a Laor disk line and narrow Fe Kα emission line. The highly ionized absorber does not introduce sufficient curvature to the continuum to significantly affect the red wing of the iron line, and we find that the inner radius of the Laor disk line model is constrained to be $r_{\rm in} < 1.9 r_g$ with 99.9% confidence (for one interesting parameter), indicating that the broad red wing of the iron line is still present. If the Fe line comes from an accretion disk truncated at the innermost stable circular orbit, this indicates a black hole spin of $a > 0.95$. In this model the radial emissivity profile is r^{-q} with $q = 3.4^{+0.1}_{-0.2}$, the disk inclination angle is $i = 42^\circ \pm 1^\circ$, and the EW of the narrow Fe Kα line is 22 eV, consistent with the *Chandra* value.

The lower inclination angle of $i = 26^\circ$ given in Table 1 results from attributing the drop in flux at 6.69 keV to the blue wing of the broad iron line rather than an absorption line. With the CCD resolution *XMM-Newton* data the $i = 26^\circ$ interpretation wants an additional emission line at 6.9 keV (Fabian et al. 2002) to account for the flux above $\gtrsim$6.7 keV. The value of $i = 42^\circ$ in our model is consistent with, e.g., model 2 of Fabian et al. (2002). Furthermore, the $i = 42^\circ$ model results in extra broad iron line flux up to $\simeq$6.9 keV and can account for the positive residuals around 6.8–6.9 keV seen, e.g., in Figure 4, which assumed an inclination of $i = 26^\circ$.

3.3. *The High-Ionization Absorber*

The highly ionized gas giving rise to the H- and He-like absorption lines may be either intrinsic to the source or serendipitously located along the line of sight. In the former case, it must be outflowing from MCG −6-30-15 at $2.0^{+0.7}_{-0.9} \times 10^3$ km s^{-1}, whereas in the latter case it would have a velocity $0.3^{+0.7}_{-0.9} \times 10^3$ km s^{-1} relative to the Galaxy.

The possibility that the absorbing gas is local is intriguing, since a number of other AGNs show iron absorption features that are kinematically consistent with a local origin (McKernan et al. 2004). In addition, O VII absorption is seen along every line of sight through the Galaxy for which we have a sufficiently high signal-to-noise ratio spectrum (Fang et al. 2003, 2005), although the O absorber need not be as highly ionized as the Fe absorber. If the H- and He-like Fe absorption seen in MCG −6-30-15 is simply due to a high-ionization phase of the interstellar medium (ISM), then we can estimate the size of the absorber. If we assume the absorber is in pressure balance with the ISM, $P/k = 10^4$ cm^{-3} (Cox & Reynolds 1987), and is collisionally ionized, $T \sim 10^7$ K, then using $P/k = nT$ implies $n = 10^{-3}$ cm^{-3}. The path length through the absorber, l, is then $l \simeq N_{\rm H}/n = 30$ Mpc for $N_{\rm H} = 10^{23}$ cm^{-2}, which is more than 3 orders of magnitude larger than the diameter of the Galaxy. If the absorber is local, then such a large column density of highly ionized material along a "random" line of sight is hard to explain.

An alternative origin for the H- and He-like absorption lines is in an outflow. MCG −6-30-15 is known to possess a complex "warm absorber" (Otani et al. 1996; Reynolds 1997; George et al. 1998; Lee et al. 2001; Turner et al. 2003, 2004) showing a broad range of ionization states and outflow velocities, and it is possible that the high-ionization absorber is at the hot and fast end of a continuum of properties within the warm absorber (Lee et al. 2002a). Warm absorber models do show components outflowing from MCG −6-30-15 at $\simeq$2000 km s^{-1} (Turner et al. 2003; Sako et al. 2003), and discrete, blueshifted absorption lines are seen, such as O VII Lyα and O VIII Lyα (outflowing at 2300 and 1900 km s^{-1}, respectively, consistent with Turner et al. 2004), and S XVI Lyα and Si XIV Lyα (2300 and 2200 km s^{-1}, respectively). Furthermore, absorption lines are seen in the HEG outflowing at intermediate velocities, such as Fe XVIII (or Ne V) at 347 km s^{-1} and Fe XXIV (or Ne IX) at 864 km s^{-1} (these are also seen with *XMM-Newton*; Turner et al. 2004). The presence of these high- and intermediate-velocity components supports the suggestion that the highly ionized absorber is associated with the warm absorber. Examples of similarly highly ionized, but higher velocity, outflows include the quasar MR 2251−178, for which the HETGS also reveals Fe XXVI absorption (Gibson et al. 2005), and the quasar PG 1211+143 (Pounds et al. 2003).

The warm absorber itself has a complex internal structure, since, for example, O VII Lyα and O VIII Lyα absorption lines are also seen at rest in the source frame (Turner et al. 2004), indicating a range of outflow velocities. Furthermore, strong absorption lines are also seen from much lower ionization species such as O I that cannot be in equilibrium with the highly ionized absorber (which is too highly ionized to contain any significant O I), indicating a range of different ionization states distributed throughout the absorber. This complexity is well known, and while the overall ionization and velocity structure of warm absorbers is unknown, it is often modeled by a number of independent, discrete "zones" that can adequately reproduce the observed spectrum.

We can estimate the mass outflow rate associated with the high-ionization component giving rise to the H- and He-like iron absorption lines using the ionization parameter, $\log \xi = 3.6$; ionizing luminosity, $L_{\rm ion} = 2 \times 10^{43}$ ergs s^{-1} (assuming $H_0 = 70$ km s^{-1} Mpc^{-1} and $q_0 = 0$); and outflow velocity, $v = 2000$ km s^{-1}. The ionization parameter $\xi = L_{\rm ion}/nr^2$ implies $nr^2 = 5 \times 10^{39}$ cm^{-1}. The mass outflow rate is then $\dot{M}_{\rm high} = \Omega nr^2 m_p v = 0.3(\Omega/4\pi)\ M_\odot$ yr^{-1}, giving a kinetic energy of $L_{\rm KE,\,high} = 4 \times 10^{41}(\Omega/4\pi)$ ergs s^{-1}, which is approximately $0.1L_{\rm X}$. We note that these estimates depend on the unknown extent to which the absorbing material is clumped. Blustin et al. (2005) find that, for MCG −6-30-15, the warm absorber has an outflow rate of $\dot{M}_{\rm WA} = 0.16\ M_\odot$ yr^{-1} and a kinetic luminosity of $L_{\rm KE,\,WA} = 10^{39}$ ergs s^{-1}. For a covering fraction of $(\Omega/4\pi) = 0.05$, the kinetic luminosity of the high-ionization component, $L_{\rm KE,\,high} = 2 \times 10^{40}$ ergs s^{-1}, dominates the energy budget of the outflow as a whole. The high-ionization component can also account for a significant fraction of the outflowing mass.

An estimate of the distance from the ionizing source can be obtained by using $N \simeq n\Delta r$, where Δr is the thickness of the absorber, and the ionization parameter $\xi = L_{\rm ion}/nr^2$, to get $r \leq 0.02(\Delta r/r)$ pc for $N = 10^{23}$ cm^{-2} (§ 3.1) and $\Delta r/r \leq 1$. This is extremely close to the central engine and implies a density of $n = 2 \times 10^6$ cm^{-3}. The corresponding timescale for variability due to the motion of the absorber is $r/v \sim 8(\Delta r/r)$ yr. We have examined the AO1 *Chandra* HETGS observation of MCG −6-30-15 (obs/433) and detect Fe XXV absorption at 6.7 keV with an EW of -16^{+0}_{-8} eV and Fe XXVI absorption at 7.0 keV with an EW of -13^{+11}_{-13} eV. (These can be seen in Fig. 5 of Lee et al. [2002b] and are consistent with the values listed in Table 2.) There is no evidence of variability in the EWs of the H- and He-like Fe lines between the AO1 observations of 2000 May 5 and August 21–22 and our more recent observations between 2004 May 19 and 27, although our measurement uncertainties do not provide strong constraints.

3.4. *Conclusions*

The *Chandra* HEG spectrum of the iron K bandpass of MCG −6-30-15 shows the following.

1. There are narrow absorption lines in the *Chandra* HEG spectrum from H- and He-like iron, requiring ion column densities of $N_{\rm Fe\ XXV} = (3 \times 10^{17})$–$(3 \times 10^{18})$ cm^{-2} for $b = 500$–100 km s^{-1}, respectively, and $N_{\rm Fe\ XXVI} = (6 \times 10^{17})$–$(4 \times 10^{19})$ cm^{-2} for $b = 500$–100 km s^{-1}, respectively. If the absorbing gas is photoionized with solar iron abundance and a velocity dispersion parameter of $b = 100$ km s^{-1}, we find $\log N_{\rm H} = 23.2$ and $\log \xi = 3.6$. The strongest two absorption lines predicted by the model between 2 and 6 keV are also detected, namely, S XVI Lyα and Si XIV Lyα.

2. The difference spectrum between the high- and low-flux states is well described by a power law in which a 6.7 keV absorption line is weakly detected, showing that the variable power-law emission also passes through the highly ionized absorber giving rise to the narrow H- and He-like absorption lines in the average spectrum.

3. Ionized absorption models, in which continuum curvature can mimic the broad red wing of the putative broad iron K line, predict iron K-shell absorption lines in the 6.4–6.6 keV range that are inconsistent with the *Chandra* HEG spectrum. In addition, the fact that the difference spectrum between the high- and low-flux states is well described by a power law strongly suggests that the curvature is not caused by absorption.

4. Applying the photoionization model used to described the H- and He-like absorption lines in the *Chandra* HEG spectrum to the *XMM-Newton* EPIC pn spectrum, we find that a broad iron line is still required. The Fe Kα emission extends down to $<1.9r_g$, and if the line comes from an accretion disk truncated at the innermost stable circular orbit, this indicates a black hole spin of $a > 0.95$.

5. The highly ionized absorber giving rise to the H- and He-like iron absorption lines in the *Chandra* HEG spectrum may be either intrinsic to the source or serendipitously located along the line of sight. In the former case it must be outflowing from MCG −6-30-15 at $2.0^{+0.7}_{-0.9} \times 10^3$ km s^{-1}, whereas in the latter it would have a velocity $0.3^{+0.7}_{-0.9} \times 10^3$ km s^{-1} relative to the Galaxy. If the absorber is intrinsic to the source, it may be a highly ionized, high-velocity component of the warm absorber. This high-ionization component would dominate the energy budget of the outflow and account for a significant fraction of the outflowing mass.

Future observations of the iron K band with *Astro-E2* will determine the velocity shift of the H- and He-like absorption lines with greater precision, help determine the location and nature of the highly ionized absorbing gas, and place stronger constraints on ionized partial-covering models. Such observations can also be used to search for multiple velocity components of absorption lines and to look for plasma diagnostics associated with the warm absorber.

We thank John Houck and Roderick Johnstone for their help with computer software, Simon Vaughan for the *XMM-Newton* spectrum, Barry McKernan and Sarah Gallagher for helpful discussions, and the anonymous referee for helpful comments and suggestions. Support for this work was provided by NASA through the Smithsonian Astrophysical Observatory (SAO) contract SV3-73016 to the Massachusetts Institute of Technology for support of the *Chandra* X-Ray Center, which is operated by the SAO for and on behalf of NASA under contract NAS 8-03060. J. C. L. thanks and acknowledges support from the *Chandra* fellowship grant PF2-30023; this is issued by the *Chandra X-Ray Observatory* Center, which is operated by SAO on behalf of NASA under contract NAS 8-39073.

REFERENCES

Behar, E., & Netzer, H. 2002, ApJ, 570, 165
Blustin, A. J., Page, M. J., Fuerst, S. V., Branduardi-Raymont, G., & Ashton, C. E. 2005, A&A, 431, 111
Cox, D. P., & Reynolds, R. J. 1987, ARA&A, 25, 303
Fabian, A. C., Iwasawa, K., Reynolds, C. S., & Young, A. J. 2000, PASP, 112, 1145
Fabian, A. C., Nandra, K., Reynolds, C. S., Brandt, W. N., Otani, C., Tanaka, Y., Inoue, H., & Iwasawa, K. 1995, MNRAS, 277, L11
Fabian, A. C., Rees, M. J., Stella, L., & White, N. E. 1989, MNRAS, 238, 729
Fabian, A. C., & Vaughan, S. 2003, MNRAS, 340, L28
Fabian, A. C., et al. 2002, MNRAS, 335, L1
Fang, T., McKee, C. F., Canizares, C. R., & Wolfire, M. 2005, ApJ, submitted
Fang, T., Sembach, K. R., & Canizares, C. R. 2003, ApJ, 586, L49
George, I. M., Turner, T. J., Netzer, H., Nandra, K., Mushotzky, R. F., & Yaqoob, T. 1998, ApJS, 114, 73
Gibson, R. R., Marshall, H. L., Canizares, C. R., & Lee, J. 2005, ApJ, 627, 83
Guainazzi, M., et al. 1999, A&A, 341, L27
Houck, J. C. 2002, in High-Resolution X-Ray Spectroscopy with *XMM-Newton* and *Chandra*, ed. G. Branduardi-Raymont (London: Mullard Space Science Laboratory), 17, http://www.mssl.ucl.ac.uk/~gbr/rgs_workshop/papers/houck_jc.ps
House, L. L. 1969, ApJS, 18, 21

Iwasawa, K., Fabian, A. C., Young, A. J., Inoue, H., & Matsumoto, C. 1999, MNRAS, 306, L19
Iwasawa, K., et al. 1996, MNRAS, 282, 1038
Kallman, T., & Bautista, M. 2001, ApJS, 133, 221
Kinkhabwala, A. A. 2003, Ph.D. thesis, Columbia Univ.
Kotani, T., Ebisawa, K., Dotani, T., Inoue, H., Nagase, F., Tanaka, Y., & Ueda, Y. 2000, ApJ, 539, 413
Krolik, J. H., & Kallman, T. R. 1984, ApJ, 286, 366
Laor, A. 1991, ApJ, 376, 90
Lee, J. C., Canizares, C. R., Fang, T., Morales, R., Fabian, A. C., Marshall, H. L., & Schulz, N. S. 2002a, in X-Ray Spectroscopy of AGN with *Chandra* and *XMM-Newton*, ed. T. Boller (MPE Rep. 279; Garching: MPE), 9
Lee, J. C., Fabian, A. C., Brandt, W. N., Reynolds, C. S., & Iwasawa, K. 1999, MNRAS, 310, 973
Lee, J. C., Fabian, A. C., Reynolds, C. S., Brandt, W. N., & Iwasawa, K. 2000, MNRAS, 318, 857
Lee, J. C., Iwasawa, K., Houck, J. C., Fabian, A. C., Marshall, H. L., & Canizares, C. R. 2002b, ApJ, 570, L47
Lee, J. C., Ogle, P. M., Canizares, C. R., Marshall, H. L., Schulz, N. S., Morales, R., Fabian, A. C., & Iwasawa, K. 2001, ApJ, 554, L13
Magdziarz, P., & Zdziarski, A. A. 1995, MNRAS, 273, 837
Marshall, H. L., Dewey, D., & Ishibashi, K. 2004, Proc. SPIE, 5165, 457
McKernan, B., Yaqoob, T., & Reynolds, C. S. 2004, ApJ, 617, 232
Mushotzky, R. F., Fabian, A. C., Iwasawa, K., Kunieda, H., Matsuoka, M., Nandra, K., & Tanaka, Y. 1995, MNRAS, 272, L9
Nandra, K., George, I. M., Mushotzky, R. F., Turner, T. J., & Yaqoob, T. 1997, ApJ, 477, 602
Nandra, K., Pounds, K. A., Stewart, G. C., Fabian, A. C., & Rees, M. J. 1989, MNRAS, 236, 39P
Otani, C., et al. 1996, PASJ, 48, 211
Pounds, K. A., Reeves, J. N., King, A. R., Page, K. L., O'Brien, P. T., & Turner, M. J. L. 2003, MNRAS, 345, 705
Reynolds, C. S. 1997, MNRAS, 286, 513
Reynolds, C. S., & Nowak, M. A. 2003, Phys. Rep., 377, 389
Reynolds, C. S., & Wilms, J. 2000, ApJ, 533, 821
Reynolds, C. S., Wilms, J., Begelman, M. C., Staubert, R., & Kendziorra, E. 2004, MNRAS, 349, 1153
Ruszkowski, M., Fabian, A. C., Ross, R. R., & Iwasawa, K. 2000, MNRAS, 317, L11
Sako, M., et al. 2003, ApJ, 596, 114
Shih, D. C., Iwasawa, K., & Fabian, A. C. 2002, MNRAS, 333, 687
Spitzer, L. 1978, Physical Processes in the Interstellar Medium (New York: Wiley)
Tanaka, Y., et al. 1995, Nature, 375, 659
Turner, A. K., Fabian, A. C., Lee, J. C., & Vaughan, S. 2004, MNRAS, 353, 319
Turner, A. K., Fabian, A. C., Vaughan, S., & Lee, J. C. 2003, MNRAS, 346, 833
Turner, T. J., Kraemer, S. B., George, I. M., Reeves, J. N., & Bottorff, M. C. 2005, ApJ, 618, 155
Vaughan, S., & Edelson, R. 2001, ApJ, 548, 694
Vaughan, S., & Fabian, A. C. 2004, MNRAS, 348, 1415
Verner, D. A., Verner, E. M., & Ferland, G. J. 1996, At. Data Nucl. Data Tables, 64, 1
Wilms, J., Reynolds, C. S., Begelman, M. C., Reeves, J., Molendi, S., Staubert, R., & Kendziorra, E. 2001, MNRAS, 328, L27